EES Catalysis

PAPER

View Article Online
View Journal

Cite this: DOI: 10.1039/d5ey00325c

Unveiling the role of oxygen species in surface promoted Fe–Mn oxides for chemical looping oxidative dehydrogenation of ethane

Dennis Chacko, Luke M. Neal, Andrew Pedersen and Fanxing Li *

Received 12th November 2025,
Accepted 29th November 2025

DOI: 10.1039/d5ey00325c

rsc.li/eescatalysis

In this study, redox catalysts composed of Fe–Mn mixed oxides with Na_2WO_4 and $Na_4Mg(WO_4)_3$ promoters are investigated for chemical looping oxidative dehydrogenation (CL-ODH) of ethane. Although $Na_4Mg(WO_4)_3$ was shown to be more effective in inhibiting CO_x formation when used to promote a Mg–Mn oxide, both promoters performed similarly for Fe–Mn mixed oxides during CL-ODH. Due to their tendency to spontaneously release lattice oxygen at the CL-ODH operating temperature range, a number of reoxidation conditions were investigated for a $Na_4Mg(WO_4)_3$ promoted $(Fe_{0.1}Mn_{0.9})_xO_y$ redox catalyst to determine the effect of the cation oxidation state. Tuning the oxidation conditions significantly improved ethylene (from 59 to 63%) and C_{2+} high-value products (from 67 to 70%) yields, which can be primarily attributed to lowered CO_x formation. From *in situ* XRD, XPS, and pulsed experiments, the inhibition of CO_x formation resulted from the lower proportion of Mn^{3+} cations, which decreased the amount of highly active lattice oxygen species responsible for CO_x formation.

Broader context

Ethylene is the most important building block in industry, with an annual production exceeding 200 million tons. However, its production by steam cracking remains one of the most carbon- and energy-intensive industrial processes, responsible for more than 300 million tons of CO_2 emissions annually. Developing routes to low-carbon ethylene is therefore essential for decarbonizing the chemical sector. Chemical looping oxidative dehydrogenation (CL-ODH) offers a promising alternative by employing lattice oxygen from redox-active oxides to selectively combust hydrogen. This approach can surpass equilibrium yield limits of thermal cracking while reducing energy demand and CO_2 intensity. Recent work has shown that oxide composition, promoters, and redox conditions strongly govern activity and selectivity. In this study, we report how mixed Fe–Mn oxides promoted with alkali tungstates can be tuned to maximize ethylene yield while suppressing CO_x formation, pointing to a promising strategy for sustainable olefin production.

Introduction

Ethylene is an important precursor for a number of materials, including polyethylene, ethylene oxide, ethylene glycol, vinyl chloride, and many others.[1] An estimated 228.5 million tons of ethylene were produced in 2023.[2] Ethylene is industrially produced using thermal cracking, catalytic cracking, and methanol to olefins, with thermal cracking accounting for over 80% of its global production.[3] The primary feedstocks for ethylene production *via* cracking are naphtha and ethane, with ethane being the predominant feedstock in North America due to shale gas production. In this process, ethane and steam are fed to a high temperature reactor (typically 850–950 °C) where ethane undergoes thermal cracking to form ethylene *via* a series of gas phase radicals, which also produces other side products and deposits coke. The thermal cracking of ethane is given below in eqn 1:

$$C_2H_6 \leftrightarrow C_2H_4 + H_2 \quad \Delta H^{850^\circ C} = 143 \text{ kJ mol}^{-1} \qquad (1)$$

There are numerous drawbacks to the steam cracking process. The single-pass ethylene yields from steam cracking are typically 52–55%, and are limited by the thermal cracking equilibrium. The production of ethylene from the steam cracking of ethane contributes an estimated 1.2 tons of CO_2 per ton of ethylene produced.[4,5] Steam cracking processes in general generate an estimated 300 million tons of global CO_2 emissions per year.[6]

Chemical looping oxidative dehydrogenation is an alternative process that uses the lattice oxygen from a reducible metal oxide-based catalyst to directly dehydrogenate ethane, or selectively combust hydrogen under thermal cracking conditions.[7–26]

Department of Chemical and Bimolecular Engineering, North Carolina State University, 911 Partners Way, Raleigh, North Carolina 27695-7905, USA. E-mail: Fli5@ncsu.edu

The catalyst is then regenerated using an oxidant such as air in a second step (or second regeneration reactor). Using this method, the single-pass ethylene yield can potentially exceed the thermal equilibrium yield, which can lower downstream compression and separation demands, energy requirements, and CO_2 emissions.

There is a great deal of literature investigating chemical looping redox catalysts for various applications, where Fe and/or Mn are the redox-active cations responsible for lattice oxygen donation and uptake.[7,10–16,18,20,22–44] The activity and selectivity of these catalysts are generally attributed to the catalyst's reducibility, as well as the near-surface concentration and oxidation state of the redox active species.[12,13,22,23,31,32,39,41,45] Hong *et al.* reported a Fe–$CeZrO_x$-based catalyst for CO_2 CL-ODH of ethane, where the surface concentration of Fe was found to correlate with the formation of CO_x through deep oxidation of surface intermediates.[32] Wang *et al.* reported a Ce-doped $LaMnO_3$ redox catalyst for CL-ODH of ethane, where Ce-modification was found to improve ethylene selectivity through the decrease of near-surface Mn^{4+}/Mn^{3+} ratio.[23] Xing *et al.* investigated a $SrMnO_3$ catalyst doped with halide ions, which were shown to improve oxygen mobility, decrease non-selective adsorbed oxygen, and increase the average Mn oxidation state, leading to higher activity for ethane dehydrogenation.[20] Luongo *et al.* reported a sequential bed chemical looping system using an M1 dehydrogenation catalyst in tandem with a Sr–Ca–Fe perovskite material for hydrogen combustion. The perovskite material is utilized for its oxygen uncoupling capability, where the oxygen carrier releases gaseous oxygen into the gas phase,[34,35,45–47] in this case to combust hydrogen. They modified the perovskite using a molten Na_2CO_3 promoter to suppress nonselective oxygen uncoupling, which would otherwise lead to CO_x formation, showing that the molten salt effectively slowed the rate of O_2 release.[18] Despite many investigations of catalysts utilizing Fe and Mn as the active components, there are few studies of mixed Fe–Mn oxides for CL-ODH. Zhang *et al.* investigated Fe–Mn mixed oxides synthesized using a green solid-state grinding method with biomass based oxygenates for the CL-ODH of ethane. Doping with xylitol resulted in increased porosity, increased oxygen vacancies, and lower Fe and Mn oxidation state, resulting in improved ethylene yield.[48] Yusuf *et al.* investigated several Fe–Mn oxides promoted with Na_2WO_4 for the CL-ODH of ethane, demonstrating the ability to alter the Fe : Mn ratio to achieve a reduction enthalpy that could satisfy the ethane thermal cracking heat requirements.[49]

Previous studies have demonstrated that Na- and W- based promoters have relatively low melting points and exhibit surface enrichment on Mn-based oxides. As a result, they suppress near-surface nonselective oxidative species while facilitating the transport of ionic oxygen species to the surface to selectively combust hydrogen.[11–14,41,49] As such, these promoted Mn-containing oxides are effective for ethane ODH through coupled gas phase ethane cracking and selective hydrogen combustion. We recently reported the use of a $Na_4Mg(WO_4)_3$ molten salt promoter with a redox-active oxide composed of Mg_6MnO_8. Using this promoter, we were able to significantly suppress the CO_x selectivity, which we attributed to a slower reduction rate and improved surface coverage of Mg_6MnO_8 at high temperature compared to promotion with Na_2WO_4.[41] In the current study, we evaluated the performance of Fe–Mn oxides with Na_2WO_4 and $Na_4Mg(WO_4)_3$ promotion under varying oxidation conditions. While the $Na_4Mg(WO_4)_3$promoter did not produce a similar effect when used with the mixed Fe–Mn oxides, we were able to demonstrate fine control of CL-ODH performance within a narrow range of reoxidation oxygen partial pressures, achieving 63–64% ethylene yield and 5–7% CO_x selectivity. Detailed characterizations, including *in situ* XRD, TGA/DSC, and XPS, were conducted to identify the active species responsible for nonselective products.

Methods and materials

Catalyst synthesis

Each of the Fe–Mn oxide catalysts was synthesized *via* the modified Pechini method. Stoichiometric amounts of $Mn(NO_3)_2{\cdot}4H_2O$ (Sigma-Aldrich, 98%) and $Fe(NO_3)_3{\cdot}9H_2O$ (Sigma-Aldrich, >99.95% trace metals basis) were dissolved in DI H_2O with stirring. Once the metal precursors were fully dissolved, citric acid was added to achieve a 2.5 : 1 molar ratio of citric acid to metal ions in the solution and heated to 50 °C with stirring for 1 hour. Following the dissolution of the citric acid, ethylene glycol was added to the solution in a molar ratio of 1.5 : 1 to the citric acid and heated to 80 °C. Once gelated, the resulting mixture was dried overnight in an 80 °C oven. Finally, the dried mixture was calcined in a still air furnace at 450 °C for 3 hours to decompose the citrate polymer, then ramped to 900 °C for 8 hours to form the final mixed metal oxide. For the samples without Fe, commercial Mn_3O_4 (Noah Technologies, Lot #0239936/1.1) was used.

The $Na_4Mg(WO_4)_3$ promoter was synthesized *via* a solid-state method, as reported in our previous study.[41,50] Briefly, stoichiometric amounts of Na_2CO_3 (Sigma Aldrich, >99.5%), $Mg(NO_3)_2{\cdot}6H_2O$ (Sigma Aldrich, 99%), and WO_3 (Sigma Aldrich, >99.9%) (2 : 1 : 3 molar ratio) were ground together in an agate mortar until a uniform, fine powdered mixture was formed. The uniform mixture then underwent calcination under a still air atmosphere, first heating to 450 °C for 5 hours to decompose the nitrates and carbonates, and then heating to 632 °C for 72 hours to form the $Na_4Mg(WO_4)_3$. The as-synthesized promoter will be abbreviated as NaMgW.

For promotion with Na_2WO_4, the $Na_2WO_4{\cdot}2H_2O$ (Sigma Aldrich, >99%, Lot #MKBZ4027V) was used. The promoter loadings were normalized to attain a final loading of 1.7 wt% Na, to achieve 10.8 wt% Na_2WO_4 and (15.9 wt% $Na_4Mg(WO_4)_3$), respectively (based upon total of promoted catalyst weight). The metal oxide and the salt promoter were added to a 50 mL stainless steel ball mill jar, and 3 mm ZrO_2 balls were added to attain a 10 : 1 weight ratio of balls to precursors. The ZrO_2 balls served as the grinding media to promote uniform mixing and intimate contact between the promoter and oxide during ball milling. After milling, the balls were removed by sieving, and

the resulting mixture was calcined in air at 900 °C for 8 hours. Zr contamination was confirmed to be negligible based on X-ray fluorescence spectroscopy. In the following sections, the catalysts will be abbreviated NaMgW–$(Fe_xMn_{1-x})_yO_z$ or NaW–$(Fe_xMn_{1-x})_yO_z$.

Reactive testing

Chemical looping oxidative dehydrogenation of ethane reaction testing. The synthesized catalysts were sieved to attain particles in the size range of 425–850 μm. 500 mg of the catalyst particles were loaded into a quartz U-tube of 8 mm O.D. and 4 mm I.D. The catalyst bed volume was measured to normalize the gas hourly space velocity (GHSV) to 4500 h^{-1}. The catalyst bed was fixed in place at the bottom of the U-tube by placing quartz wool on either side. The U-tube was then filled with α-Al_2O_3 grit on each side of the catalyst bed. The U-tube was placed into a reactor furnace to heat it to each respective operating temperature. The catalytic activity for ethane oxidative dehydrogenation (ODH) was evaluated using redox cycles. The setup for the CL-ODH catalyst activity testing is represented in Fig. 1. Initially, the catalysts underwent two break-in cycles at 900 °C in an 80% H_2/Ar mixture, to stabilize the physical and chemical properties prior to ODH cycling. Each cycle included a reduction step (3 minutes in H_2/Ar) and a reoxidation step (3 minutes in 20% O_2/Ar), with a 5-minute argon purge between each half-cycle. After completing the break-in cycles, the catalysts were tested under CL-ODH conditions. For this, a 5 mL injection of ethane (80% C_2H_6/Ar) was introduced into the reactor, followed by a 5-minute purge with 100% Ar. The catalysts were then reoxidized with 17% O_2/Ar for 3 minutes, with a final 5-minute purge with 100% Ar.

The catalyst bed volume, density, and flow rates for each step are given for all of the catalysts in Table S1. The products from the reduction steps were collected in a Tedlar gas sampling bag and characterized using a gas chromatograph (Agilent Technologies 7890B). The gas chromatograph is equipped with a flame ionization detector (FID) for analysis of the hydrocarbon products, and Ar and He thermal conductivity detectors (TCD) channels for H_2 and CO/CO_2, respectively. The conversion of ethane, and the selectivities of each of the carbonaceous species were calculated based on the carbon mass balance. The total hydrogen expected was calculated from the hydrogen mass balance from the measured hydrocarbons. The hydrogen conversion was calculated based on the difference between the total expected hydrogen and the hydrogen measured *via* the TCD. To quantify coke formation, the effluent gas composition was monitored during the reoxidation step using a quadrupole mass spectrometer (MKS Cirrus II) in all the experiments performed. The reported selectivities are adjusted to include the coking selectivity.

The NaMgW–$(Fe_{0.1}Mn_{0.9})_xO_y$ catalyst was selected for additional experiments with varying oxidation conditions. The rationale for these oxidation conditions is discussed in greater depth in later sections. The conditions for the reduction half-cycle were the same as for the other tests. This catalyst was subjected to reoxidation half-cycles with the same reoxidation time using 4.3% O_2/Ar and 10.8% O_2/Ar. It was also subjected to reoxidation half-cycles using 17% O_2/Ar, but halving the reoxidation time to 90s. Additionally, the catalyst was subjected to identical reoxidation conditions (17% O_2/Ar for 3 minutes), with 20 minutes of inert purging following the reoxidation.

C_2H_4–H_2 co-feed pulse experiments

To evaluate the selectivity of hydrogen combustion *vs.* ethylene overoxidation to CO_x, the NaMgW–$(Fe_{0.1}Mn_{0.9})_xO_y$ was selected to undergo C_2H_4–H_2 pulse experiments. 100 mg of the catalyst in the 425–850 μm range was packed into a quartz U-tube (8 mm O.D., 4 mm I.D.). The catalyst bed was fixed in place at the bottom of the U-tube by placing quartz wool on either side. The U-tube was then filled with α-Al_2O_3 grit on each side of the catalyst bed. The U-tube was placed into a reactor furnace to heat it to 850 °C. The catalyst was pretreated with 17% O_2/Ar for 30 minutes to ensure it was fully oxidized. After this, the reactor was purged with 100% Ar for 5 minutes. Then the catalyst was subjected to 50, 1 mL pulses of 80% C_2H_4/20% H_2. This number of pulses was calculated to be sufficient for the exhaustion of the catalyst's maximum oxygen capacity. The catalyst's maximum oxygen capacity was calculated using the theoretical weight change from the bixbyite phase to the monoxide solid-state solution. Then the catalyst was reoxidized in 10% O_2/Ar,

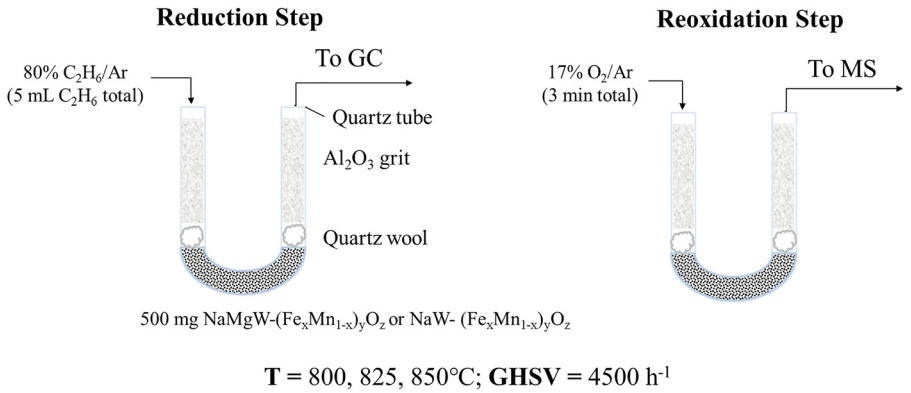

Fig. 1 Schematic for CL-ODH catalyst activity testing.

and again subjected to the same pulses, and finally reoxidized in 4% O_2/Ar before being subjected to the pulses again. The pulses were fed to the reactor using a Vici Valco 6-way valve, where C_2H_4 and H_2 were fed into a 1 mL sample loop using Alicat mass flow controllers. The sample loop was filled for 2 minutes, and then the contents of the loop was injected to the reactor for 2 minutes using 100% Ar (25 sccm).

H_2-temperature programmed reduction

H_2 temperature programmed reduction was performed with each of the catalysts using a TA Instruments SDT Q600. Approximately 10–30 mg of each catalyst was loaded into the instrument using alumina crucibles. The samples were heated to 850 °C for 30 minutes in 20% O_2/Ar to ensure a clean catalyst. After this, the catalysts were cooled to 500 °C, and held in 20% O_2/Ar for 10 minutes to ensure they were fully oxidized to bixbyite ($(Fe_xMn_{1-x})_2O_3$). These conditions were selected to replicate oxidation with air. The gas flow was switched to 100% Ar for an additional 10 minutes to purge out the remaining O_2 before switching to 5% H_2/Ar. The temperature was held at 500 °C for 10 minutes, before ramping to 900 °C (5 °C min^{-1}) and holding at the final temperature for an additional 10 minutes. Following the TPR, the samples were cooled to 850 °C in 100% Ar with a ramp rate of 5 °C min^{-1}. The samples were then reoxidized at 850 °C in 20% O_2/Ar for 20 minutes. The gas flow was finally switched to 100% Ar and the temperature was held at 850 °C for an additional 60 minutes to observe if any oxygen uncoupling occurs under the inert purge. The weight loss and derivative weight loss with respect to temperature were normalized to the initial total weight of the samples following the pretreatment.

TGA/DSC redox cycling. Redox cycling was performed with the promoted-$(Fe_{0.1}Mn_{0.9})_xO_y$ catalysts using a TA Instruments SDT Q600. Approximately 10–30 mg of each catalyst was loaded into the instrument using alumina crucibles. The samples were heated to 850 °C for 30 minutes in 20% O_2/Ar to ensure a clean and fully oxidized catalyst. The gas flow was switched to 100% Ar for an additional 10 minutes to purge out the remaining O_2 before beginning 5 redox cycles. Each cycle consisted of a 10-minute reduction with 5% H_2/Ar and a 10-minute reoxidation with 17% O_2/Ar, with 11 minutes of purging with Ar between each step. For the NaMgW–$(Fe_{0.1}Mn_{0.9})_2O_3$ sample, the catalyst was first subjected to a 5% H_2/Ar pretreatment for 30 minutes at 850 °C, then reoxidized with 4.3% O_2/Ar for 30 minutes. The catalyst was then subjected to 5 redox cycles using varying oxygen partial pressure for reoxidation (4.3% O_2/Ar, then 10% O_2/Ar, and finally 17% O_2/Ar). The resulting heat flows were normalized so the cumulative sum of the heat released during redox cycles was equal to the lower heating value for H_2. Additional details for the DSC computation are given in the SI.

Characterization

X-ray diffraction. The crystal structures of the prepared and cycled catalysts were identified using X-ray diffraction. An Empyrean X-ray diffractometer was used to analyze the phases of the catalysts for both *ex situ* and *in situ* experiments, with a radiation source of CuKα (λ = 0.1542 nm) operated at 45 kV and 40 mA. For *ex situ* XRD, a scan range of 2θ = 10–90° was used with a 0.025° step size.

In situ XRD experiments were also conducted for the promoted $(Fe_{0.1}Mn_{0.9})_xO_y$ catalysts. The catalysts were scanned for a 2θ range of 10–80°, with a step size of 0.04°. Each catalyst was first heated to 500 °C in air before being subjected to similar conditions as the TGA TPR mentioned above, with 3% H_2/N_2. Following the TPR, the catalyst was then purged with 100% N_2 for 10 minutes and then reoxidized under various oxygen concentrations specified in Fig. 6. For NaW–$(Fe_{0.1}Mn_{0.9})_2O_3$, the catalyst was regenerated with 17% O_2/N_2 for 30 minutes, and then subjected to 2 redox cycles with 3% H_2/N_2. Each redox cycle consisted of 15 minutes of 3% H_2/N_2, and a 30-minute reoxidation with 17% O_2/N_2, with 10 minutes of 100% N_2 purging between steps. For the NaMgW–$(Fe_{0.1}Mn_{0.9})_xO_y$ catalyst, after the TPR the catalyst was subjected to redox cycling with increasing P_{O_2} (first regenerating with 4% O_2/N_2, then 10% O_2, then 17% O_2/N_2). The reduction half-cycles were the same as for the NaW–$(Fe_{0.1}Mn_{0.9})_xO_y$ catalyst. Following the last redox cycle, each catalyst was regenerated in air (21% O_2/N_2) for 30 minutes and cooled to room temperature in 100% N_2. The *in situ* XRD experiments were performed using the Empyrean X-ray diffractometer with an Anton-Parr XRK-900 reactor chamber. XRD scans of the powder were taken during heating to 500 °C, to 850 °C, under redox cycling at 850 °C, and cooling back to room temperature.

X-ray photoelectron spectroscopy. The near-surface (~1–3 nm) composition and Fe and Mn oxidation states of the unpromoted $(Fe_{0.1}Mn_{0.9})_xO_y$, NaW-promoted, NaMgW-promoted, and several cycled catalysts were collected using X-ray photoelectron spectroscopy. NaMgW–$(Fe_{0.1}Mn_{0.9})_xO_y$ catalyst samples were evaluated after cycling under the standard conditions, cycling with 10% O_2/Ar reoxidation, and cycling with 20 minutes of 100% Ar purge following reoxidation with 17% O_2/Ar. The cycled catalysts were all immediately sealed and quenched following cycling to prevent additional oxidation or uncoupling. The catalysts were mounted on the sample holder in a N_2-filled glovebox and loaded into the load-lock using a N_2-filled bag.

The XPS measurements were conducted using a PHI 3057 XPS system with a spherical capacitor analyzer (PHI 80-865A), and a dual anode X-ray source (PHI 04-548). The sample powders were mounted on Cu tape and then placed into the load-lock at 10^{-5} torr to remove moisture. The samples were finally moved into the analysis chamber on a tilting stage. The chamber was pumped by a PerkinElmer TNBX ion pump, and each sample achieved a base pressure of at 10^{-9} torr or less. Monochromatic Al Kα radiation was utilized.

The subsequent binding energies were calibrated to the C 1s peak at 284.8 eV. Multiplex scans of C 1s, O 1s, Mg 1s, Fe 2p, Mn 2p, Na 1s, and W 4d were recorded using a 23.50 eV pass energy and a step size of 0.025 eV. Each region was scanned 10 times, with an additional 10 scans for species with low surface concentration. The Mn 2p spectra were deconvoluted using CasaXPS (Casa Software, Ltd, U.K.) to roughly evaluate the Mn oxidation state for each of the catalysts.

Results and discussion

Phase verification

The XRD of the unpromoted Fe–Mn, NaW-promoted, and NaMgW-promoted catalysts are summarized in Fig. 2. Following calcination, non-Fe containing Mn_3O_4 (Fig. 2a) mostly oxidizes to Mn_2O_3 with trace Mn_3O_4 remaining. The promoted Mn oxide catalysts primarily consist of the promoters and Mn_2O_3, however the NaMgW-promoted catalyst also contains a small amount of Na_2WO_4, (see Fig. S1 for an enlarged image).[41] The $(Fe_{0.1}Mn_{0.9})_xO_y$ catalysts (Fig. 2b) are similar, giving patterns generally consistent with $(Fe_{0.1}Mn_{0.9})_2O_3$. We note that $Fe_{0.266}Mn_{1.734}O_3$ has the closest Fe : Mn ratio of the reference patterns available in the PDXL database. A small amount of Fe_3O_4 is also observed for the NaMgW-promoted sample. For the $(Fe_{0.2}Mn_{0.8})_xO_y$ catalysts (Fig. 2c), there are some additional phases observed, in addition to $(Fe_{0.2}Mn_{0.8})_2O_3$. There are also peak shifts (2θ = 18.78, 27.15, 32.44, and 49.23°) which suggests substitution of Mn^{4+} for Mg^{2+} in $Na_4Mg(WO_4)_3$, which has been reported previously for this material.[51] For the NaW-promoted catalyst, a trace amount of Mn_2O_3 is also observed. For the $(Fe_{0.6}Mn_{0.4})_xO_y$ catalysts (Fig. 2d), they are also oxidized to the $(Fe_{0.6}Mn_{0.4})_2O_3$ following calcination, with some Fe_2O_3 observed for the unpromoted catalyst. However, for the NaMgW-promoted catalyst, no crystalline Mg- or W-containing phases were observed following the calcination. Instead, minority phases such as Fe_2O_3, Mn_3O_4, and some $NaMnO_2$ are observed. The NaW–$(Fe_{0.6}Mn_{0.4})_xO_y$ consists only of the Na_2WO_4 and $(Fe_{0.6}Mn_{0.4})_2O_3$. The formation of the bixbyite $(Fe_xMn_{1-x})_2O_3$ phase upon calcination in air at 900 °C is consistent with the reported phase behavior of the Fe–Mn–O system.[52,53]

Reactive performance for chemical looping – oxidative dehydrogenation

Without promotion, mixed Fe–Mn oxides near exclusively generate undesirable CO_x products. The CL-ODH performance of each of the promoted Fe–Mn catalysts is summarized in Fig. 3. Similar trends between the catalysts seem to hold for the ethane conversion throughout the tested temperature range. The promoted $(Fe_{0.2}Mn_{0.8})_xO_y$ catalysts exhibited the highest activity and highest ethylene yields (63% ethylene yield for NaW–$(Fe_{0.2}Mn_{0.8})_xO_y$), consistent with what was previously reported by Yusuf *et al.*[49] The pure Mn oxide catalysts exhibit the highest selectivity, but the lowest activity for both ethane and hydrogen conversion. Hydrogen conversion is a key parameter for satisfying the net system energy demand and relaxing

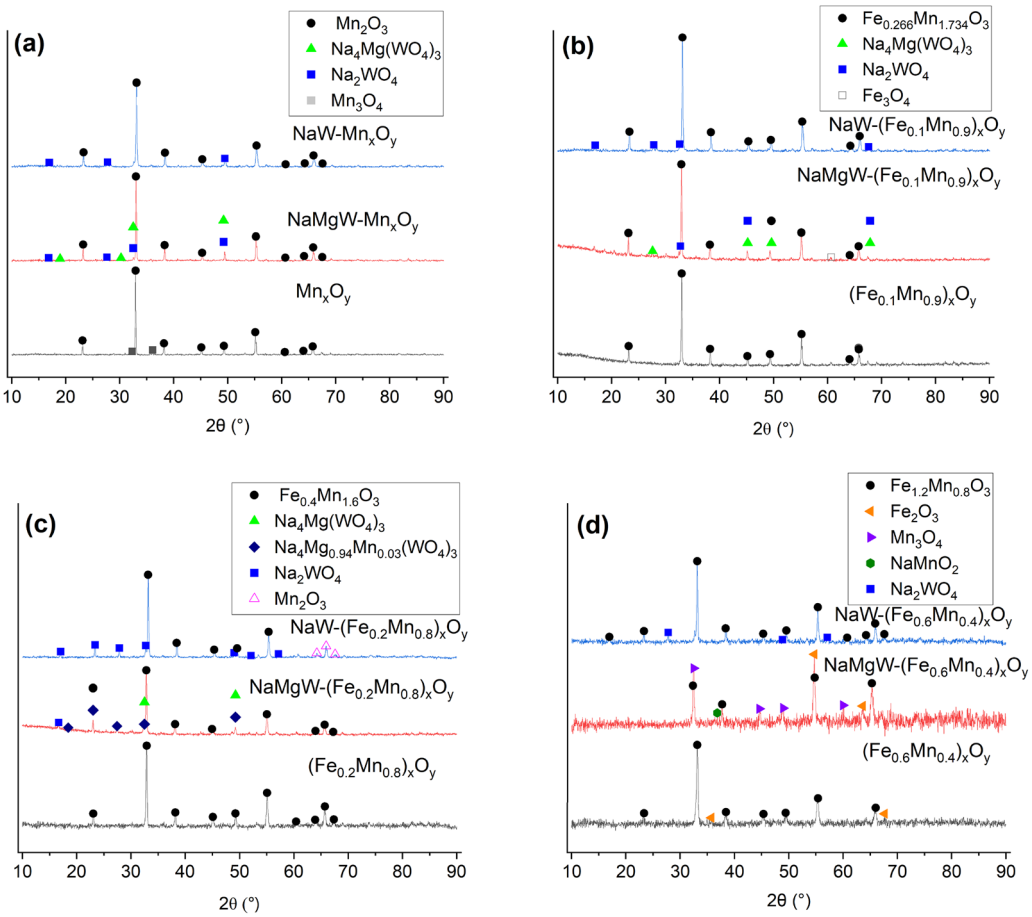

Fig. 2 *Ex situ* XRD of synthesized (a) Mn_xO_y, (b) $(Fe_{0.1}Mn_{0.9})_xO_y$, (c) $(Fe_{0.2}Mn_{0.8})_xO_y$, and (d) $(Fe_{0.6}Mn_{0.4})_xO_y$ catalysts.

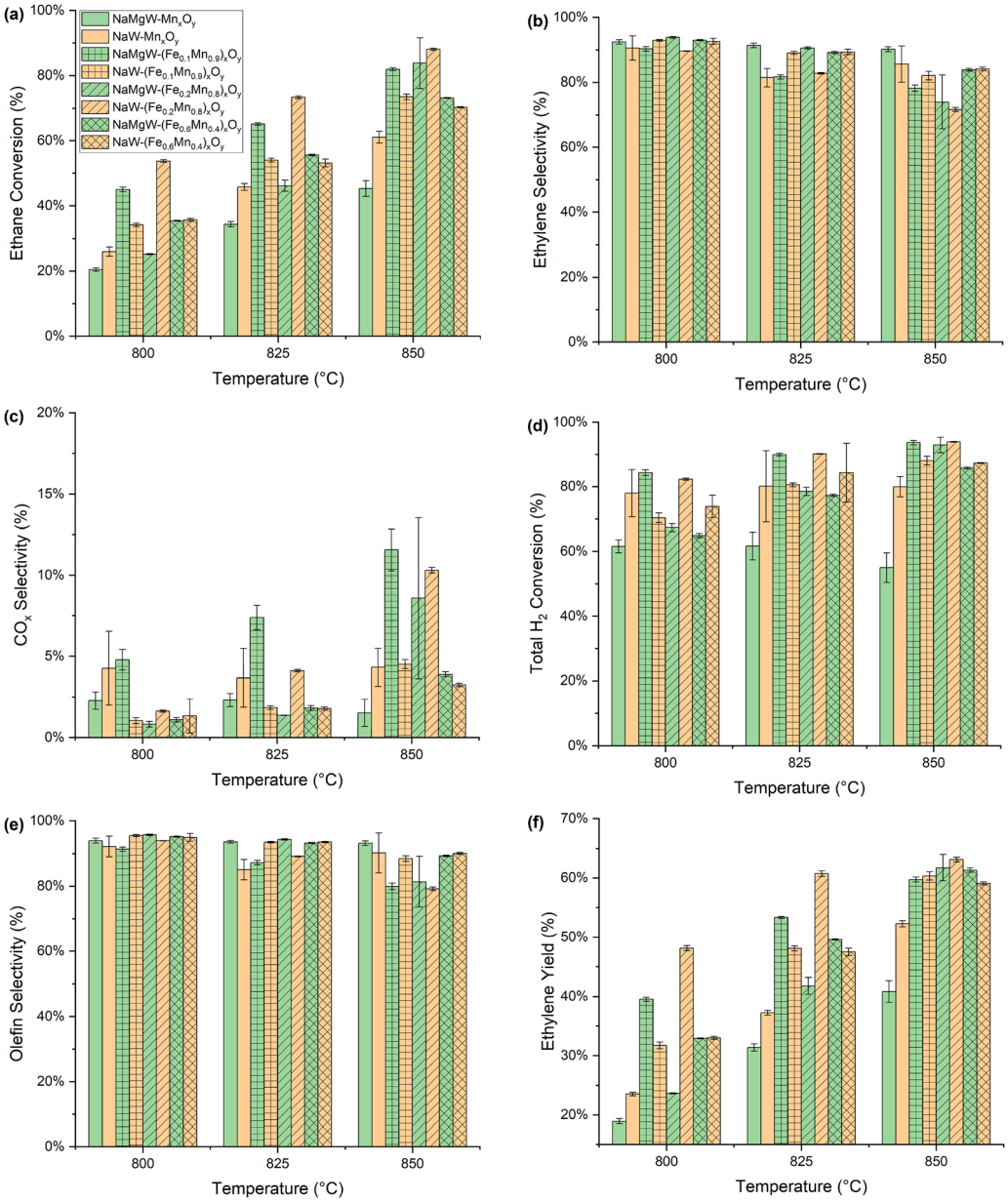

Fig. 3 (a) Ethane conversion, (b) ethylene selectivity, (c) CO_x selectivity, (d) H_2 conversion, (e) total olefin selectivity, and (f) ethylene yield for NaW- and NaMgW-promoted catalysts at 800, 825, and 850 °C with GHSV = 4500 h^{-1}.

the equilibrium conversion limit.[10–12] Furthermore, the NaMgW-promoted Mn oxide catalyst was significantly less active than the NaW-promoted Mn oxide catalyst. Despite not observing any crystalline Mg- or W-containing phases, the NaMgW–$(Fe_{0.6}Mn_{0.4})_xO_y$ catalyst performed somewhat comparably to the equivalent NaW-promoted catalyst. In general, the Fe–Mn catalysts exhibit similar ethylene yield at 850 °C (59–61%). Moreover, promotion with NaMgW did not yield a significant decrease in CO_x selectivity, especially for the $(Fe_{0.1}Mn_{0.9})_xO_y$ catalyst (5–11% CO_x selectivity). This is despite the *ex situ* XRD indicating that the $Na_4Mg(WO_4)_3$ phase was preserved following calcination for the Mn_xO_y, $(Fe_{0.1}Mn_{0.9})_xO_y$, and $(Fe_{0.2}Mn_{0.8})_xO_y$ catalysts.

The similar CO_x selectivity between NaW- and NaMgW-promoted contrasts with our previous study: NaMgW was demonstrated to suppress CO_x formation by improving surface coverage and slowing the reduction rate at high temperature for a Mg–Mn mixed oxide catalyst. Further evaluation of the redox characteristics and surface enrichment are therefore conducted to elucidate the cause of the different CL-ODH performance. Additional details regarding the product distributions, including coking selectivity are provided in Table S2.

Evaluation of the redox behavior

The results of the H_2 TPR and reoxidation are summarized in Fig. 4. The catalysts generally are fully oxidized to the bixbyite

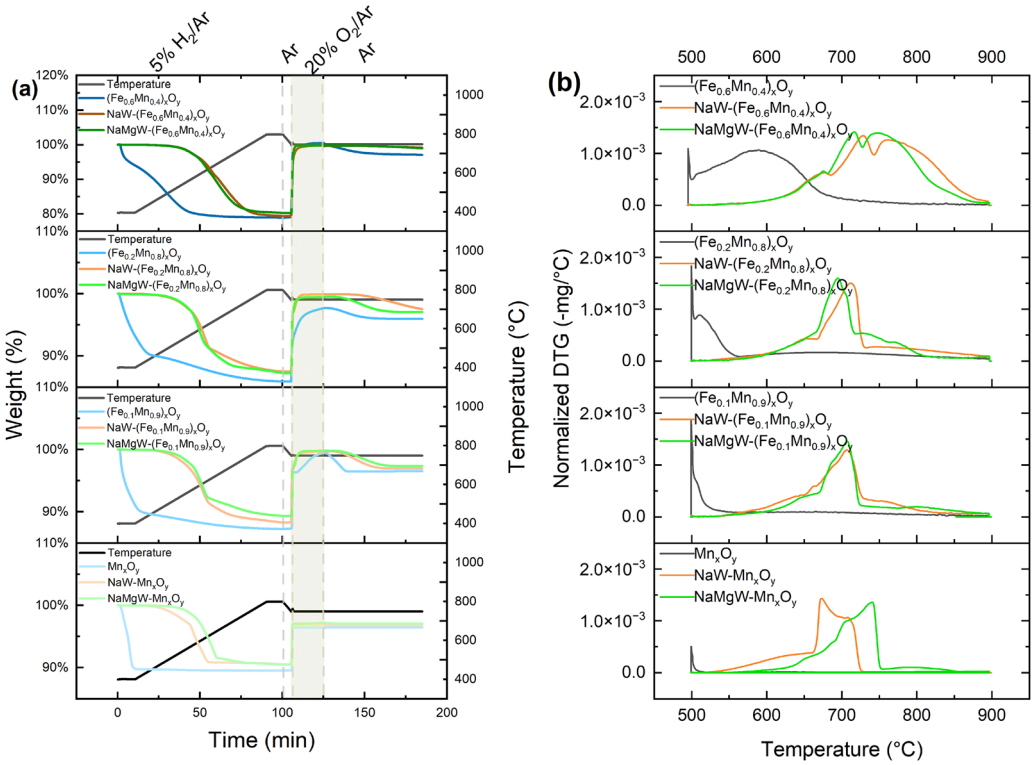

Fig. 4 (a) Weight change during H_2 TPR, reoxidation, and inert purge and (b) normalized derivative weight change during H_2 TPR for promoted and unpromoted Fe–Mn catalysts.

phase ($(Fe_xMn_{1-x})_2O_3$; space group *Ia3*) following the pretreatment at 500 °C. During the reduction the catalysts reduce first to the spinel phase ($(Fe_xMn_{1-x})_3O_4$; space group *Fd3m*), followed by reduction to a monoxide solid-state solution (FeO–MnO), and possible reduction to metallic Fe. For the unpromoted catalysts, most of the reduction occurs at 500 °C, prior to the temperature ramp. This may occur from the reduction of bixbyite. For the Fe-containing samples, the promoted catalysts exhibit very similar reduction rates and oxygen capacities. The weight changes observed for each Fe–Mn catalyst is consistent with reduction to monoxide and reoxidation back to $(Fe_xMn_y)_2O_3$, except for the $(Fe_{0.6}Mn_{0.4})_xO_y$ catalysts, where the weight change indicates a fraction of the Fe cations reduce to metallic Fe. In contrast, the pure Mn oxide catalysts quickly reduce from Mn_2O_3 to MnO, but only reoxidize to Mn_3O_4, indicating that 20% O_2 in Ar is insufficient to regenerate Mn_2O_3 at 850 °C. This incomplete reoxidation is consistent with its lower CL-ODH activity. DTG shows that higher Fe:Mn ratios result in decreased catalyst reducibility, which corresponds with the decreased activity observed for the $(Fe_{0.6}Mn_{0.4})_xO_y$ catalysts during CL-ODH testing. For the promoted Mn_xO_y catalysts, the NaMgW-promoted sample exhibits a higher reduction onset temperature than NaW–Mn_xO_y, consistent with its lower ethane conversion. For the promoted $(Fe_{0.2}Mn_{0.8})_xO_y$ and $(Fe_{0.6}Mn_{0.4})_xO_y$ redox catalysts, the reduction behavior is very similar for both promoters, with the NaW-promoted catalyst skewing towards slightly higher temperatures. The $(Fe_{0.1}Mn_{0.9})_xO_y$ catalyst exhibits an early onset reduction temperature, likely corresponding to reduction from bixbyite to spinel, which subsequently reduces to a monoxide solid-state solution. Despite the NaMgW-promoted $(Fe_{0.1}Mn_{0.9})_xO_y$ exhibiting higher activity and lower olefin selectivity for CL-ODH, its reduction extent and rate are slightly lower than those of the NaW equivalent. Further insight can be gleaned from the reoxidation and subsequent purging with inert gas. The addition of Fe also enables reoxidation to the bixbyite phase in air at high temperature, unlike the Mn oxide catalysts. However, the NaMgW–$(Fe_{0.2}Mn_{0.8})_xO_y$, NaMgW–$(Fe_{0.1}Mn_{0.9})_xO_y$, and NaW–$(Fe_{0.1}Mn_{0.9})_xO_y$ catalysts fully decompose to the spinel phase within ~40 minutes of inert purging. Considering that the purge time following the oxidation during our typical packed-bed CL-ODH experiments is only 5 minutes, it is possible that the oxides are still readily decomposing (also known as uncoupling) during the ethane ODH step,[35] releasing appreciable amounts of active lattice oxygen into the gas phase. The observed oxygen uncoupling (*i.e.* oxide decomposition) rate under inert gas flow also suggests that higher Fe concentration stabilizes the bixbyite phase. Based on the observation of this facile redox behavior, we decided to probe the effect of reoxidation and/or purging conditions, which affect the starting oxidation states of Mn and Fe in the CL-ODH step. With this in mind, NaMgW–$(Fe_{0.1}Mn_{0.9})_xO_y$ was selected for further CL-ODH testing with varying oxidation conditions, considering its especially high observed CO_x selectivity.

Reactive performance with varying oxidation conditions

Based upon the TPR results indicating potential influence from the oxygen uncoupling behavior, differing oxidation conditions were selected based on the potential active oxygen species present during CL-ODH conditions. From the inert purge following the reoxidation after the H_2 TPR, an additional 20-minute purge was selected, as the decomposition/uncoupling rate slows significantly over this amount of inert purging. Based upon the weight change (~2.65 wt%), it is likely that, during the inert purge, the material decomposes from bixbyite to spinel. Lower partial oxygen pressures (4.3% and 10.8% O_2) were selected from the Mn oxide phase diagrams, as these are equivalent to the equilibrium partial pressure for the conversion of Mn_2O_3 to Mn_3O_4 at 800 and 850 °C, respectively.[54] The higher oxygen partial pressure of 17% was chosen for comparison with a previous study using Na_2WO_4.[49] To the best of the authors' knowledge, there are no studies that evaluate the phase behavior of the Fe–Mn–O system over a range of P_{O_2} applicable to the operating temperature range and Fe:Mn ratios evaluated in this study. Finally, a 90s reoxidation time with 17% O_2/Ar was used, as it was calculated to be roughly equivalent to the minimum oxygen required to regenerate the bixbyite after reduction to spinel.

The CL-ODH results from the varied oxidation conditions are summarized in Fig. 5. Each of the milder re-oxidation conditions effectively lower the CO_x selectivity significantly. The additional post-oxidation purge results in the smallest decrease, likely due to incomplete decomposition to the spinel phase within this time. At 800 °C, both 4 and 10% O_2 likely reoxidize the Fe–Mn oxide to the same oxidation state, as is reflected by the similar CL-ODH results at this temperature. Both shortening the reoxidation or using 10% O_2/Ar proved to be effective at lowering the CO_x selectivity while still maintaining a high ethylene yield at 850 °C (63% ethylene yield with 7% CO_x selectivity and 64% ethylene yield with 5% CO_x selectivity, respectively). This represents a marked improvement over the standard operating conditions, which exhibited ~60% ethylene yield and 11.6% CO_x selectivity at the same temperature. It is also observed that there is not an appreciable drop off in ethane or hydrogen conversion, suggesting that the metastable oxygen species present during the standard oxidation conditions may not be selective for hydrogen combustion. More detailed product selectivities are provided in Table S2. Ethylene selectivity and ethane conversion for all of the catalysts are summarized in Fig. S2. Further characterization will be discussed in the following sections to further elucidate the species present under varying oxidation conditions and their impact on the CL-ODH performance.

Effects of promoters and oxidation conditions on active species

To further elucidate the metal oxide species present during CL-ODH conditions, *in situ* XRD was performed on the

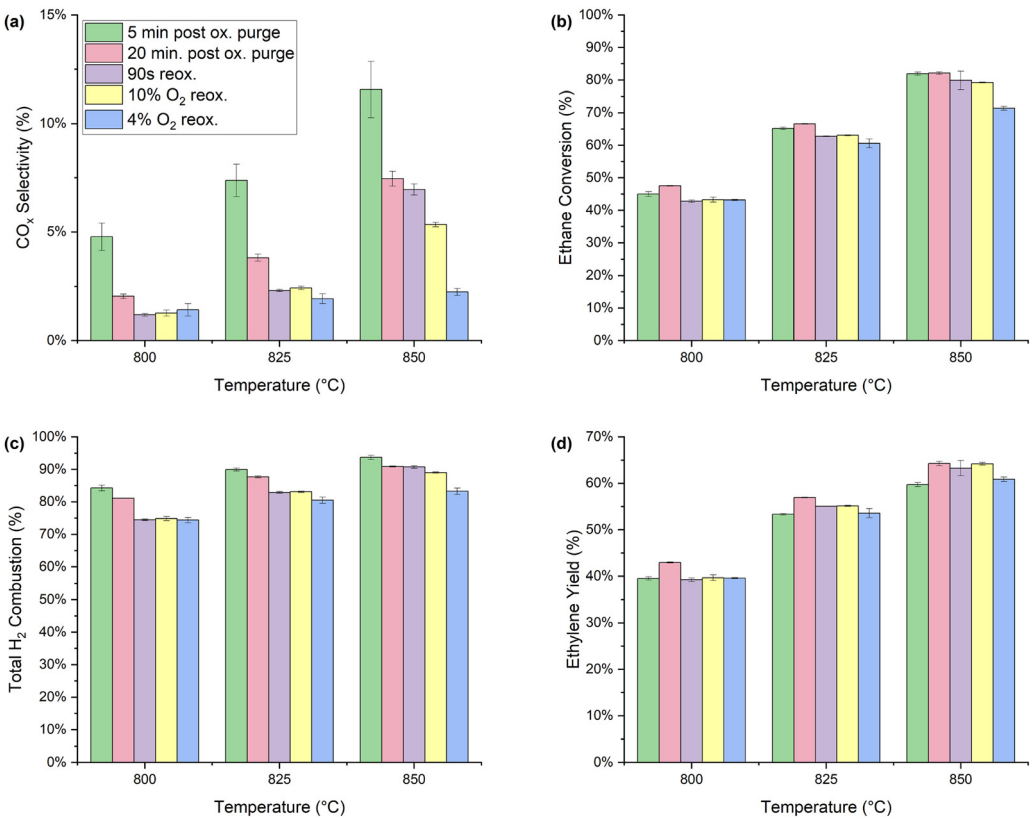

Fig. 5 (a) CO_x selectivity, (b) ethane conversion, (c) total H_2 combustion, and (d) ethylene yield results from NaMgW–$(Fe_{0.1}Mn_{0.9})_xO_y$ under various oxidation conditions: (green) 5 min. post oxidation purge, (pink) 20 min. post oxidation purge, (purple) 90s reoxidation, (yellow) 10% O_2/Ar reoxidation, and (blue) 4% O_2/Ar reoxidation.

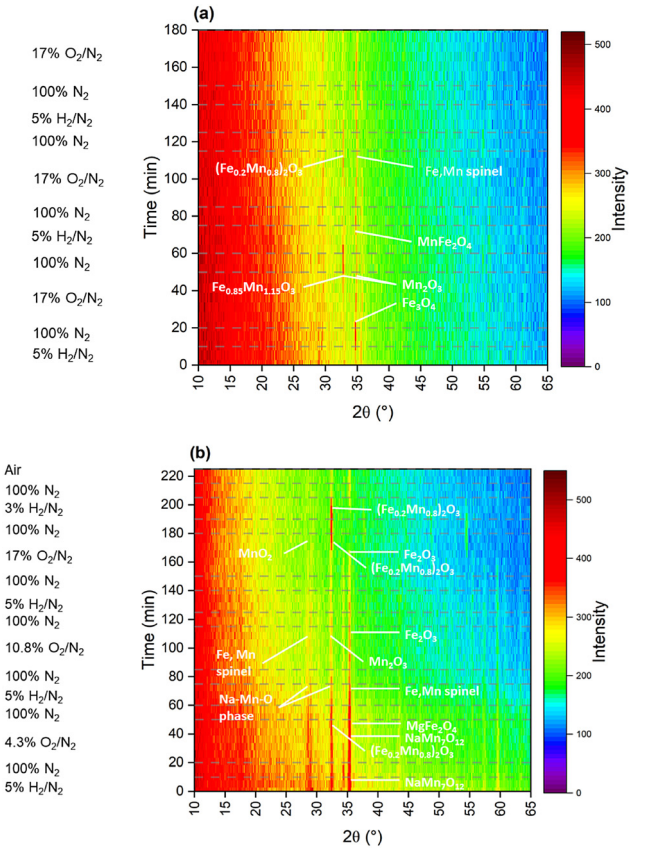

Fig. 6 *In situ* XRD of (a) NaW–$(Fe_{0.1}Mn_{0.9})_xO_y$ and (b) NaMgW–$(Fe_{0.1}Mn_{0.9})_xO_y$ subjected to 5% H_2 redox cycles at 850 °C. FeO and MnO phases form during reduction but the intensity is too low to be distinguishable on this scale.

NaMgW- and NaW-promoted $(Fe_{0.1}Mn_{0.9})_xO_y$ catalysts. The results of the *in situ* XRD for both catalysts during the redox cycling at 850 °C are shown in Fig. 6. We note that most alkali metal containing tungstate salts have melting points much lower than this temperature, and hence they are not detectable under *in situ* XRD. During the initial TPR, the oxide reduces to Fe–Mn spinel, Fe_3O_4, and then FeO, while also forming some Fe–W–O compounds. After being reoxidized, Mn_2O_3, $Fe_{0.85}Mn_{1.15}O_3$ (higher Fe : Mn ratio than the initial oxide), and some Na_xMnO_2 form. In subsequent cycling, it reduces again to Fe–Mn spinel, as well as FeO–MnO, and some Na–Mn–O compounds. The phases observed for the subsequent reduction and regeneration are similar. Finally, upon reoxidizing and cooling in inert, the catalyst primarily consists of $(Fe_xMn_y)_2O_3$ with a lower Fe:Mn ratio, in addition to Fe_2O_3, and Fe_2WO_6. Crystalline Na_2WO_4 was not detected upon cooling, but could present in an amorphous form. This is consistent with the previously reported catalyst, NaW–$(Fe_{0.2}Mn_{0.8})_xO_y$, where the crystalline Na_2WO_4 phase was no longer observed *via* XRD after cycling, instead forming (Fe,Mn)WO_4, $NaFe(WO_4)_2$, and $NaFeO_2$.[49]

The *in situ* XRD of NaMgW–$(Fe_{0.1}Mn_{0.9})_xO_y$ is shown in Fig. 6(b). At the start of the temperature programmed reduction, the catalyst initially consists of $(Fe_{0.1}Mn_{0.9})_2O_3$, $Na_4Mg_{1-2x}Mn_x(WO_4)_3$, Na_xMnO_2, and $Na_2W_4O_{13}$. During the temperature programmed reduction, it slowly progresses to FeO–MnO, Fe–Mn spinel, Mn_3O_4, Mn_3WO_6, and $NaMn_7O_{12}$. During the later stages of the reduction, some Mg–Mn and Mg–Fe spinel phases ($MgMn_2O_4$ (space group *Pbcm*) and $MgFe_2O_4$ (space group *Fd3m*)) can also be observed. Following reoxidation with 4.3% O_2, Fe–Mn spinel, Fe_3O_4, Mn_3O_4, and $NaMn_7O_{12}$ were observed. During the first reduction half-cycle, some spinel is preserved, with some reduction to FeO, MnO, and some Na–Mn–O phases. There are trace amounts of Mg–Mn and Mg–Fe spinel phases towards the end of the reduction stage. Upon reoxidation with 10% O_2/N_2, a mixture of $(Fe_{0.1}Mn_{0.9})_2O_3$, Fe_2O_3, Mn_2O_3, and Fe–Mn spinel is formed, with a small amount of Na–Mn–O and Na–Fe–O phases. In the subsequent reduction, there is mostly Mn_3O_4, FeO, MnO, with a small amount of Na–Mn–O, Mg–Mn–O, and Mg–Fe–O phases. When reoxidized with 17% O_2/N_2, it almost completely converts to a mixed Fe-Mn bixbyite phase, Fe_2O_3, with a small amount of MnO_2. During the subsequent reduction, the Fe–Mn phase is mostly still preserved, with some reduction to Fe–Mn spinel, as well as some Na_xMnO_2 and $Fe(WO_4)$ phases. Following regeneration in air and cooling to room temperature to inert, many phases are present, including $Fe_{0.85}Mn_{1.15}O_3$, Fe_2O_3, Fe_3O_4, and small amounts of Na_2WO_4, $Na_4Mg(WO_4)_3$, and $Na_xFe_yMn_zO_2$ phases. It is clear that the differing oxygen partial pressures result in mixtures of Fe–Mn oxides with different average oxidation states. The nonselective oxidation observed during CL-ODH is consistent with the formation of bixbyite and possibly even higher oxidation state Mn phases, which are generated during the reoxidation with P_{O_2} = 0.17 atm.

Due to the clear difference in CL-ODH results under differing oxidation conditions, XPS was conducted for the unpromoted, NaW-promoted, and NaMgW-promoted and cycled $(Fe_{0.1}Mn_{0.9})_xO_y$ catalysts to further evaluate the active species and surface promotion. Table 1 summarizes the near-surface atomic concentrations of each of the metals in these catalysts on a C- and O-free basis, which were computed from Mg 1s, Fe 2p, Mn 2p, Na 1s, and W $4f_{7/2}$ signals. Detailed peak fitting information for each of these peaks, as well as C1s and O 1s are given in Tables S4–S9. Each of the promoted catalysts is Na- and W-surface-enriched, with the Mn near-surface concentration being suppressed. All of the cycled catalysts exhibit a decrease in surface Mn concentration compared to the fresh catalyst. Moreover, each of the catalysts has little to no near-surface Mg, suggesting that Mg possibly migrates into the oxygen carrier core. This may result from the formation of Mg–Mn and Mg–Fe spinel phases, which were observed under the lower P_{O_2} reoxidation conditions during *in situ* XRD. Based on the *in situ* XRD and *ex situ* XRD of the cycled catalysts (Fig. S4), some $Na_4Mg(WO_4)_3$ is still present, but some other Na- and W-containing phases also form. This suggests that while some $Na_4Mg(WO_4)_3$ may still be present during or after cycling, other phases are preferentially dispersed on the catalyst surface. This could explain the lack of CO_x suppression under the standard cycling conditions when compared to the previously reported NaMgW–Mg_6MnO_8 catalyst.[41]

We also observe that the cycled samples with lowered oxidations have higher near-surface Fe. This suggests that there

Table 1 Near-surface at% as determined by XPS on a carbon and oxygen free basis. The relative surface enrichment of the metals are listed in parentheses by dividing the XPS measured near surface cation concentration with its nominal concentration from the bulk composition

Surface at% (C, O free)	Mg	Fe	Mn	Na	W	$\frac{Na}{W}$	$\frac{Fe}{Mn}$	$\frac{Na+W}{Fe+Mn}$
$(Fe_{0.1}Mn_{0.9})_xO_y$	—	7.26% (0.73)	92.74% (1.03)	—	—	—	0.078	—
NaW–$(Fe_{0.1}Mn_{0.9})_xO_y$ (fresh)	—	3.97% (0.44)	60.22% (0.73)	16.39% (2.75)	19.42% (6.52)	0.844	0.066	0.558
NaMgW–$(Fe_{0.1}Mn_{0.9})_xO_y$ (fresh)	0.00% (0.00)	3.43% (0.43)	59.73% (0.83)	19.71% (1.95)	17.13% (2.26)	1.151	0.057	0.583
NaMgW–$(Fe_{0.1}Mn_{0.9})_xO_y$ (17% O_2 cycled)	3.80% (1.51)	3.12% (0.39)	42.96% (0.60)	30.73% (3.05)	19.40% (2.56)	1.584	0.073	1.088
NaMgW–$(Fe_{0.1}Mn_{0.9})_xO_y$ (10% O_2-cycled)	0.00% (0.00)	3.87% (0.48)	39.80% (0.55)	30.62% (3.04)	25.71% (3.40)	1.191	0.097	1.290
NaMgW–$(Fe_{0.1}Mn_{0.9})_xO_y$ (cycled −20 min post ox. purge)	0.00% (0.00)	4.72% (0.59)	35.74% (0.50)	31.47% (3.12)	28.07% (3.71)	1.121	0.132	1.471

is a greater amount of exposed Fe phases, which may be due to the formation of the Na–Fe–O, Na–Fe–W–O, and Fe–W–O phases. For each of the samples, the peak position of the Fe $2p_{3/2}$ peaks is the same, and reasonably fitted with one peak at ~711 eV, consistent with Fe^{3+}.[55] The fresh NaW-promoted catalyst has a Na : W ratio lower than 1 (despite still being Na- and W-surface enriched), suggesting that other W-containing phases are formed in the near-surface, which is consistent with the previous study.[49] Additionally, the cycled NaMgW-promoted catalysts have a higher Na : W ratio than 1. Although the Na:W ratio for $Na_4Mg(WO_4)_3$ is ~1.33, the lack of near-surface Mg suggests this ratio cannot result from this phase, while the ratio resulting from $Na_2W_4O_{13}$ would be ~0.5. This indicates the surface must also be enriched with other Na-containing phases besides $Na_4Mg(WO_4)_3$ and $Na_2W_4O_{13}$.

While Mn 2p spectra is often used to determine the oxidation states of Mn cations in literature, an in-depth XPS study by Ilton *et al.* showed that the Mn 2p fitting parameters developed from reference Mn compounds are unable to accurately estimate the oxidation state for mixed oxidation state Mn compounds,[56] which is also consistent with our own studies. In contrast, the binding energy difference in Mn 3s multiplet splitting is proven to be a much more reliable indicator of Mn average oxidation state. The peak positions and estimated Mn oxidation state are summarized in Table 2, and the plots are shown in Fig. S3.

Following calcination, the Mn in the fresh catalysts appears to be slightly more oxidized, which is consistent with spinel and a small amount of bixbyite. The presence of a higher oxidation state Fe–Mn phase is feasible considering the fresh catalyst was calcined in still air. The catalyst cycled with 17% O_2 maintains this oxidation state. This is generally consistent with both the higher ratio of bixbyite to spinel and monoxide species observed during *in situ* XRD and the nonselective oxidation observed during CL-ODH. This is consistent with the uncoupling behavior observed during the reoxidation following TPR for both promoted catalysts, and the near-surface may also be slightly more reduced than the bulk phase. The catalyst cycled with 10% O_2/Ar has a slightly lower Mn oxidation state, consistent with Mn near the surface being present in the spinel phase (average Mn oxidation state = 2.67). Although the post-reoxidation purge duration was selected to result in reduction to spinel, the Mn oxidation state is lower, suggesting there is further reduction to monoxide in the near-surface. Overall, these results suggest that the suppression of near-surface Mn and maintaining a lower Mn oxidation state is crucial for achieving highly selective ethane ODH performance.

To further probe the impact of the higher Mn oxidation state, pulsed experiments were conducted using the NaMgW–$(Fe_{0.1}Mn_{0.9})_xO_y$ catalyst using 1 ml 80% C_2H_4/20% H_2 pulses. The results of these experiments are summarized in Fig. 7. Beyond the first 10 pulses, which are summarized in Fig. 7b (corresponding to ~1–1.8 wt% donation), the H_2 conversion and C_2H_4 converted to CO_2 are quite similar. Within the first few pulses, the catalyst pretreated with 17% O_2/Ar has appreciably higher H_2 and C_2H_4 conversion, with significantly more C_2H_4 being converted to CO_2. While the H_2 conversion is slightly higher throughout the 50 pulses, it is initially less selective to H_2 combustion in the first few pulses. It should be noted that this is within the range of O donation which is typically observed during CL-ODH (1.1 wt% in the first 5 pulses *vs.* 1.8 wt% lattice oxygen release observed during CL-ODH). These results indicate that a higher proportion of bixbyite observed from the *in situ* XRD leads to higher activity but lower selectivity due to non-selective oxidation.

Effects of promoters and oxidation conditions on the enthalpy of reduction

The selected promoted catalysts were subjected to redox cycling using TGA/DSC to evaluate their enthalpy of reduction. In the

Table 2 Mn 3s XPS peak positions and the calculated (average) Mn oxidation states

Sample	Peak 1 (eV)	Peak 2 (eV)	ΔBE	Est. average Mn oxidation state
$(Fe_{0.1}Mn_{0.9})_xO_y$	83.28	88.77	5.49	2.77
NaW–$(Fe_{0.1}Mn_{0.9})_xO_y$ (fresh)	83.31	88.85	5.54	2.71
NaMgW–$(Fe_{0.1}Mn_{0.9})_xO_y$ (fresh)	83.25	88.74	5.49	2.77
NaMgW–$(Fe_{0.1}Mn_{0.9})_xO_y$ (17% O_2-cycled)	82.90	88.40	5.50	2.76
NaMgW–$(Fe_{0.1}Mn_{0.9})_xO_y$ (10% O_2-cycled)	83.01	88.61	5.60	2.64
NaMgW–$(Fe_{0.1}Mn_{0.9})_xO_y$ (cycled −20 min post oxidation purge)	82.68	88.67	5.99	2.19

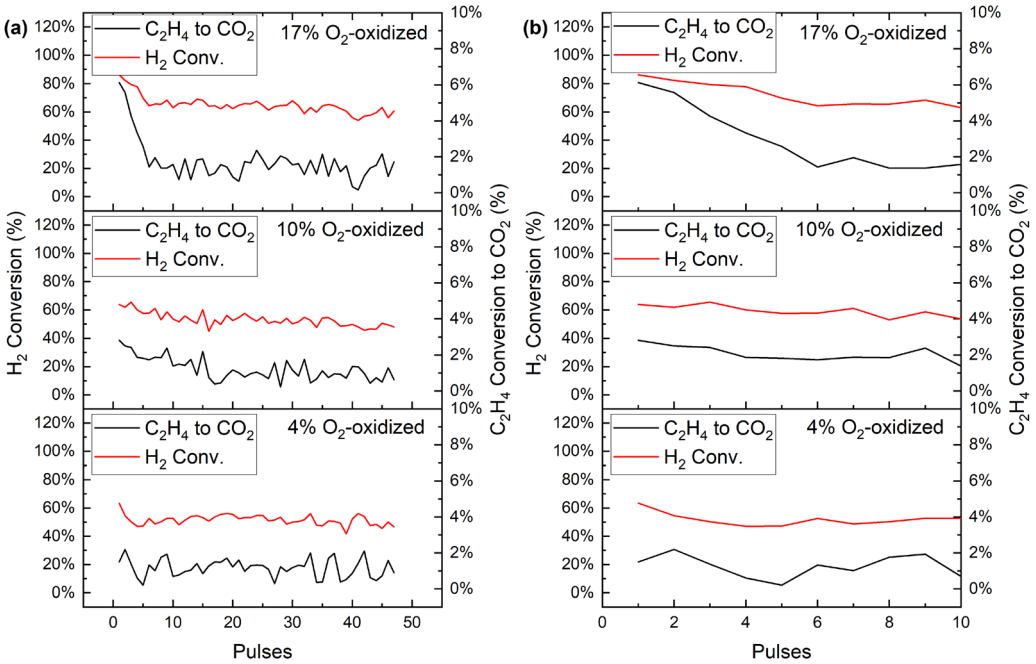

Fig. 7 (a) C_2H_4 conversion to CO_2 and H_2 conversion over all 50 pulses and (b) over the first 10 pulses with the NaMgW–$(Fe_{0.1}Mn_{0.9})_xO_y$ catalyst at 850 °C, using 80% C_2H_4/20% H_2 1 mL pulses.

previous study, it was shown that over a certain range of oxygen donation, the Fe–Mn oxides could potentially fulfill the heat demand for ethane thermal cracking in the ODH step alone.[49] Generally, the lower Fe : Mn ratio is attributed to less

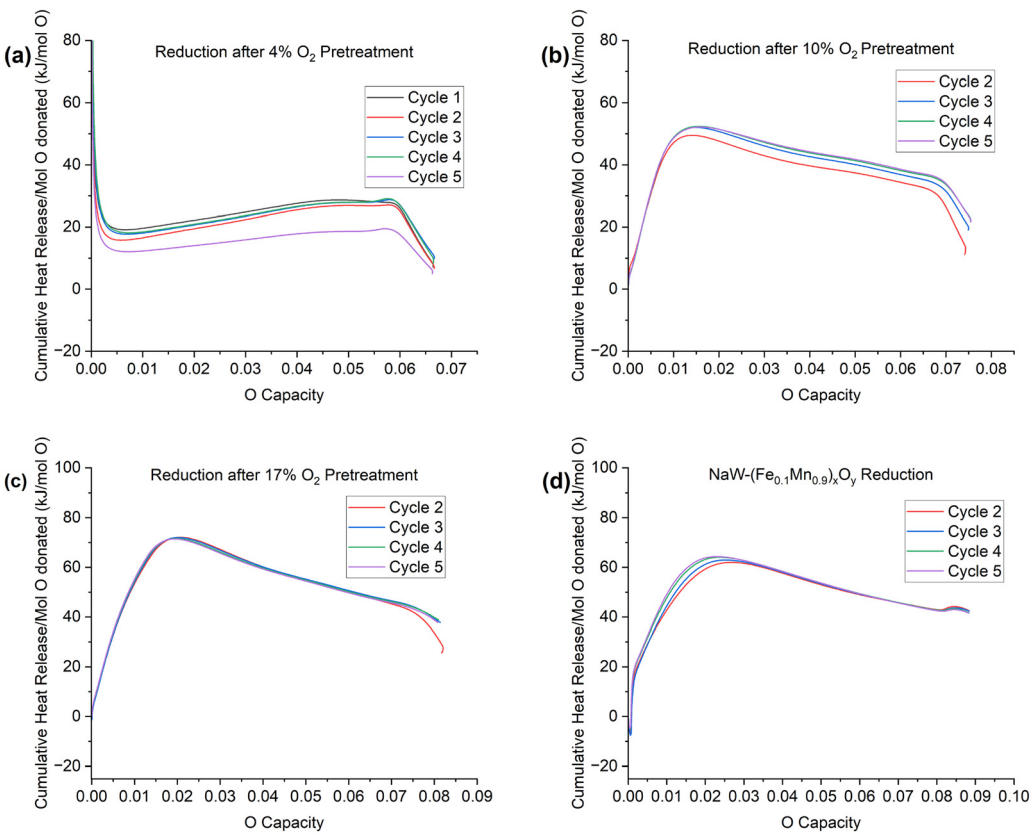

Fig. 8 Average heat release/mol O donated for (a) NaMgW–$(Fe_{0.1}Mn_{0.9})_xO_y$ cycled with 4% O_2, (b) cycled with 10% O_2, (c) cycled with 17% O_2, and (d) NaW–$(Fe_{0.1}Mn_{0.9})_xO_y$ cycled with 17% O_2.

Table 3 Reduction enthalpy observed during TGA/DSC redox cycling with H_2

Sample	Average heat of reduction[a] (kJ mol^{-1})
NaW–$(Fe_{0.1}Mn_{0.9})_xO_y$ (17% O_2 cycled)	−41.85
NaMgW–$(Fe_{0.1}Mn_{0.9})_xO_y$ (17% O_2 cycled)	−40.52
NaMgW–$(Fe_{0.1}Mn_{0.9})_xO_y$ (10% O_2 cycled)	−22.32
NaMgW–$(Fe_{0.1}Mn_{0.9})_xO_y$ (4% O_2-cycled)	−9.03

[a] The overall heat of reaction in the DSC measurement cycle was calibrated by the lower heating value of hydrogen.

endothermic reduction, as the reduction of Fe_3O_4 to FeO with H_2 is endothermic (28.85 kJ mol^{-1} O). The NaMgW-promoted catalyst was also subjected to redox cycling under each of the oxygen partial pressures investigated for CL-ODH.

The results are summarized in Fig. 8, with the reduction enthalpy averaged from cycles 2–5 in Table 3. The heat release for the reduction over time is also summarized in Fig. S4. The calculations for the average heat of reduction and cumulative heat release are described in the SI. For each of the catalysts, the reduction is initially exothermic. This may result from the reduction of bixbyite or Mn_3O_4 to MnO. Both of the catalysts cycled with 17% O_2 exhibit very similar heat release during the reduction. For the NaMgW-promoted catalyst, each of the reductions eventually becomes endothermic (Fig. S5). Although none of the redox catalysts exhibit enough heat release to fully offset the heat demand for ethane thermal cracking (143 kJ mol^{-1} O at 850 °C), they all have cumulative exotherms for the entire O donation range (Table 3) to partially offset the heat requirement. We note that the overall ODH and regeneration cycle remain to be net exothermic. That said, decreasing the endothermicity in the ODH step is nonetheless desirable since it can decrease the catalyst circulation rate and/or lower the temperature difference between the two interconnected reactors.

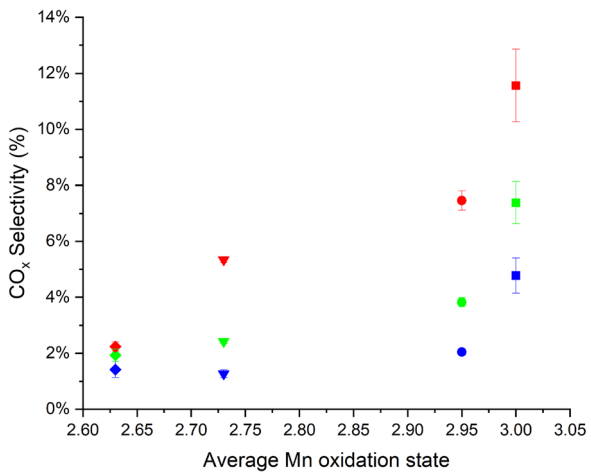

Fig. 9 CO_x selectivity *vs.* computed average starting Mn oxidation state for 4% O_2 reoxidation (diamond), 10% O_2 reoxidation (triangle), 20 min (circle). post oxidation purge, and (square) 5 min. post oxidation purge at (blue) 800 °C, (green) 825 °C, and (red) 850 °C. Note that a few error bars are too small to be clearly visible.

To further evaluate the relationship between the Mn active species and selective oxidation, the average Mn oxidation state was computed for NaMgW–$(Fe_{0.1}Mn_{0.9})_xO_y$ from the TPR and TGA redox cycling. The average Mn oxidation state from the 20 minute post oxidation purged catalyst was estimated from the weight change during the post oxidation purge of the TPR. The average Mn oxidation state for the 4% and 10% O_2 reoxidation samples was estimated using the weight change during the TGA redox cycles. It was assumed that the catalyst was fully reduced to the monoxide solid-state solution. The relationship between CO_x selectivity and the average Mn oxidation state is visualized in Fig. 9. It is observed that the CO_x selectivity is roughly correlated with the Mn oxidation state. This further corroborates that the bixbyite phases which are present during more oxidizing conditions contribute primarily to CO_x formation. Taking into account the findings from the CL-ODH experiments and pulsed experiments, it is clear that adjusting the oxidation conditions allows for the tuning of the activity and selectivity *via* the regeneration of selective Mn redox active species.

Conclusions

This study investigates mixed Fe–Mn oxides of varying ratios promoted with Na_2WO_4 and $Na_4Mg(WO_4)_3$ for chemical looping – oxidative dehydrogenation of ethane (CL-ODH). Although $Na_4Mg(WO_4)_3$ was shown to be more effective than Na_2WO_4 in inhibiting CO_x formation when used to promote a Mg–Mn oxide, $Na_4Mg(WO_4)_3$ is not a more effective promoter for mixed Fe–Mn oxides. This is due to strong Mg–Mn–Fe phase interactions, as confirmed by *in situ* XRD and XPS analysis. Nonetheless, the surface was still Na- and W-surface enriched, with suppressed concentrations of near-surface Mn cations, a key feature for mitigating CO_x formation compared to unpromoted oxides.

Further investigation of the various mixed oxide redox catalysts, particularly NaMgW–$(Fe_{0.1}Mn_{0.9})_xO_y$, indicates that altering the re-oxidation conditions or the purge time between the two CL-ODH steps would enable more precise control of the cation oxidation states, which has a direct impact towards the CL-ODH performance. For instance, using 10 vol% O_2 (as opposed to 17%) or increasing the inert purge time substantially improved the ODH performance, resulting in 36–54% reduction in CO_x selectivity on a relative basis while increasing the single-pass ethylene yields at 850 °C. Through XPS and *in situ* XRD characterizations, it was determined that maintaining a higher proportion of spinel phase as opposed to bixbyite phase after re-oxidation enhances ethylene selectivity. Under all regeneration conditions tested, the catalysts exhibited exothermicity for H_2 combustion, thereby favoring the ethane ODH reaction. These findings provide fundamental insights into the role of cation oxidation states in generating non-selective oxygen species, while also offering practical strategies to tune CL-ODH operating conditions for optimized reaction performance.

Conflicts of interest

There are no conflicts to declare.

Data availability

Data supporting this article have been included as part of the supplementary information (SI). Supplementary information is available. See DOI: https://doi.org/10.1039/d5ey00325c.

Acknowledgements

This work was supported by the National Energy Technology Lab (DE-FE0032513) and the US National Science Foundation (Award No. CBET-1923468). The characterization was performed in part at the Analytical Instrumentation Facility (AIF) at North Carolina State University which is supported by the State of North Carolina and the National Science Foundation (award number ECCS-2025064). AIF and SMIF are members of the North Carolina Research Triangle Nanotechnology Network (RTNN), a site in the National Nanotechnology Coordinated Infrastructure (NNCI).

References

1 Humans, I. W. G. on the E. of C. R. to. Ethylene, Some Industrial Chemicals, International Agency for Research on Cancer, 1994.
2 Ethylene production capacity globally 2023. Statista. https://www.statista.com/statistics/1067372/global-ethylene-production-capacity/ (accessed 2025-08-05).
3 C. Jiang, F. He, L. Zhang, G. Wang and L. Liu, Trends in Industrial Ethylene Production: Innovation in Process and Catalyst Design, *Chem. Catal.*, 2025, **5**(1), 101241, DOI: 10.1016/j.checat.2024.101241.
4 T. Ren, M. Patel and K. Blok, Olefins from Conventional and Heavy Feedstocks: Energy Use in Steam Cracking and Alternative Processes, *Energy*, 2006, **31**(4), 425–451, DOI: 10.1016/j.energy.2005.04.001.
5 Chemicals. IEA. https://www.iea.org/energy-system/industry/chemicals (accessed 2024-06-20).
6 I. Amghizar, J. N. Dedeyne, D. J. Brown, G. B. Marin and K. M. V. Geem, Sustainable Innovations in Steam Cracking: CO2 Neutral Olefin Production, *React. Chem. Eng.*, 2020, **5**(2), 239–257, DOI: 10.1039/C9RE00398C.
7 L. M. Neal, V. P. Haribal and F. Li, Intensified Ethylene Production *via* Chemical Looping through an Exergetically Efficient Redox Scheme, *iScience*, 2019, **19**, 894–904, DOI: 10.1016/j.isci.2019.08.039.
8 L. M. Neal, S. Yusuf, J. A. Sofranko and F. Li, Oxidative Dehydrogenation of Ethane: A Chemical Looping Approach, *Energy Technol.*, 2016, **4**(10), 1200–1208, DOI: 10.1002/ente.201600074.
9 V. P. Haribal, L. M. Neal and F. Li, Oxidative Dehydrogenation of Ethane under a Cyclic Redox Scheme – Process Simulations and Analysis, *Energy*, 2017, **119**, 1024–1035, DOI: 10.1016/j.energy.2016.11.039.
10 Y. Gao, X. Wang, J. Liu, C. Huang, K. Zhao, Z. Zhao, X. Wang and F. Li, A Molten Carbonate Shell Modified Perovskite Redox Catalyst for Anaerobic Oxidative Dehydrogenation of Ethane, *Sci. Adv.*, 2020, **6**(17), eaaz9339, DOI: 10.1126/sciadv.aaz9339.
11 S. Yusuf, L. Neal, V. Haribal, M. Baldwin, H. H. Lamb and F. Li, Manganese Silicate Based Redox Catalysts for Greener Ethylene Production *via* Chemical Looping – Oxidative Dehydrogenation of Ethane, *Appl. Catal., B*, 2018, **232**, 77–85, DOI: 10.1016/j.apcatb.2018.03.037.
12 S. Yusuf, L. Neal, Z. Bao, Z. Wu and F. Li, Effects of Sodium and Tungsten Promoters on Mg6MnO8-Based Core–Shell Redox Catalysts for Chemical Looping—Oxidative Dehydrogenation of Ethane, *ACS Catal.*, 2019, **9**(4), 3174–3186, DOI: 10.1021/acscatal.9b00164.
13 S. Yusuf, L. M. Neal and F. Li, Effect of Promoters on Manganese-Containing Mixed Metal Oxides for Oxidative Dehydrogenation of Ethane *via* a Cyclic Redox Scheme, *ACS Catal.*, 2017, **7**(8), 5163–5173, DOI: 10.1021/acscatal.7b02004.
14 J. Liu, S. Yusuf, D. Jackson, W. Martin, D. Chacko, K. Vogt-Lowell, L. Neal and F. Li, Redox Oxide@molten Salt as a Generalized Catalyst Design Strategy for Oxidative Dehydrogenation of Ethane *via* Selective Hydrogen Combustion, *Appl. Catal., A*, 2022, **646**, 118869, DOI: 10.1016/j.apcata.2022.118869.
15 Y. Gao, L. M. Neal and F. Li, Li-Promoted $La_xSr_{2-x}FeO_{4-\delta}$ Core–Shell Redox Catalysts for Oxidative Dehydrogenation of Ethane under a Cyclic Redox Scheme, *ACS Catal.*, 2016, **6**(11), 7293–7302, DOI: 10.1021/acscatal.6b01399.
16 Y. Gao, F. Haeri, F. He and F. Li, Alkali Metal-Promoted $La_xSr_{2-x}FeO_{4-\delta}$ Redox Catalysts for Chemical Looping Oxidative Dehydrogenation of Ethane, *ACS Catal.*, 2018, **8**(3), 1757–1766, DOI: 10.1021/acscatal.7b03928.
17 I. I. Mishanin, A. N. Kalenchuk, K. I. Maslakov, V. V. Lunin, A. E. Koklin, E. D. Finashina and V. I. Bogdan, Oxidative Dehydrogenation of Ethane over a Mo–V–Nb–Te–O Mixed-Oxide Catalyst in a Cyclic Mode, *Kinet. Catal.*, 2017, **58**(2), 156–160, DOI: 10.1134/S0023158417020094.
18 G. Luongo, F. Donat, A. H. Bork, E. Willinger, A. Landuyt and C. R. Müller, Highly Selective Oxidative Dehydrogenation of Ethane to Ethylene *via* Chemical Looping with Oxygen Uncoupling through Structural Engineering of the Oxygen Carrier, *Adv. Energy Mater.*, 2022, **12**(23), 2200405, DOI: 10.1002/aenm.202200405.
19 P. Novotný, S. Yusuf, F. Li and H. H. Lamb, Oxidative Dehydrogenation of Ethane Using MoO_3/Fe_2O_3 Catalysts in a Cyclic Redox Mode, *Catal. Today*, 2018, **317**, 50–55, DOI: 10.1016/j.cattod.2018.02.046.
20 Z. Xing, H. Chen, M. Mao, X. Liang, D. Song, Y. Li, T. Long, X. Chen and F. He, Halide Ions Doped $SrMnO_3$ for Chemical Looping Oxidative Dehydrogenation of Ethane, *Greenhouse Gases: Sci. Technol.*, 2023, **14**(4), 659–675, DOI: 10.1002/ghg.2254.

21 L. Ping, Y. Zhang, B. Wang, M. Fan, L. Ling and R. Zhang, Unraveling the Surface State Evolution of IrO_2 in Ethane Chemical Looping Oxidative Dehydrogenation, *ACS Catal.*, 2023, **13**(2), 1381–1399, DOI: 10.1021/acscatal.2c05770.

22 L. Xiaocen, W. Xuemei, X. Zifan, M. Min, S. Da, L. Yang, L. Tao, Z. Yuchao, C. Peili and H. Fang, Impact of B-Site Cations of MgX_2O_4 (X = Cr, Fe, Mn) Spinels on the Chemical Looping Oxidative Dehydrogenation of Ethane to Ethylene, *J. Fuel Chem. Technol.*, 2024, **52**(7), 1006–1019.

23 J. Wang, X. Liang, Z. Xing, H. Chen, Y. Li, D. Song and F. He, Ce-Doped $LaMnO_3$ Redox Catalysts for Chemical Looping Oxidative Dehydrogenation of Ethane, *Catalysts*, 2023, **13**(1), 131, DOI: 10.3390/catal13010131.

24 G. Hu, Z. Yu, Y. Liu, Y. Wang and Q. Guo, Molybdenum-Promoted $CuMn_2O_4$ Oxygen Carrier for Chemical Looping Oxidative Dehydrogenation of Ethane, *Ind. Eng. Chem. Res.*, 2024, **63**(20), 9018–9025, DOI: 10.1021/acs.iecr.4c00767.

25 H. Chen, Z. Xing, D. Song, X. Yu, Y. Li and F. He, Binary Li/Na Tungstates Modified Mg_6MnO_8 as Redox Catalysts for Enhanced Performance of Chemical Looping Oxidative Dehydrogenation of Ethane, *Chem. Eng. J.*, 2024, **485**, 150146, DOI: 10.1016/j.cej.2024.150146.

26 X. Tian, C. Zheng, F. Li and H. Zhao, Co and Mo Co-Doped Fe_2O_3 for Selective Ethylene Production *via* Chemical Looping Oxidative Dehydrogenation, *ACS Sustainable Chem. Eng.*, 2021, **9**(23), 8002–8011, DOI: 10.1021/acssuschemeng.1c02726.

27 J. Huang, K. Zhao, S. Jiang, S. Kang, Y. Lin, Z. Huang, A. Zheng and Z. Zhao, Heteroatom-Doping Regulated Mg_6MnO_8 for Improving C^{2+} Hydrocarbons during Chemical Looping Oxidative Coupling of Methane, *Fuel Process. Technol.*, 2022, **235**, 107352, DOI: 10.1016/j.fuproc.2022.107352.

28 T. Wang, Y. Gao, Y. Liu, M. Song, J. Liu and Q. Guo, Core-Shell Na2WO4/CuMn2O4 Oxygen Carrier with High Oxygen Capacity for Chemical Looping Oxidative Dehydrogenation of Ethane, *Fuel*, 2021, **303**, 121286, DOI: 10.1016/j.fuel.2021.121286.

29 Y. Tian, P. R. Westmoreland and F. Li, $CaMn_{0.9}Ti_{0.1}O_3$ Based Redox Catalysts for Chemical Looping – Oxidative Dehydrogenation of Ethane: Effects of Na_2MoO_4 Promoter and Degree of Reduction on the Reaction Kinetics, *Catal. Today*, 2023, **417**, 113725, DOI: 10.1016/j.cattod.2022.04.026.

30 R. Pérez-Vega, A. Abad, F. García-Labiano, P. Gayán, L. F. de Diego, M. T. Izquierdo and J. Adánez, Chemical Looping Combustion of Gaseous and Solid Fuels with Manganese-Iron Mixed Oxide as Oxygen Carrier, *Energy Convers. Manage.*, 2018, **159**, 221–231, DOI: 10.1016/j.enconman.2018.01.007.

31 D. Zhang, Y. Zhang, X. Tian and M. Ding, Chemical Looping Oxidative Dehydrogenation of Ethane over Fe-Co/HZSM-5 Redox Catalyst, *Fuel*, 2024, **363**, 130842, DOI: 10.1016/j.fuel.2023.130842.

32 S. J. Hong, B. H. Seo and J. W. Bae, Chemical Looping-Based Oxidative Dehydrogenation of Ethane and Successive CO2 Activation on Fe-Modified CeZrOx Mixed-Metal Oxides, *Energy Fuels*, 2025, **39**(30), 14752–14764, DOI: 10.1021/acs.energyfuels.5c00947.

33 P. Moldenhauer, A. Serrano, F. Garcia-Labiano, L. F. de Diego, M. Biermann, T. Mattisson and A. Lyngfelt, Chemical-Looping Combustion of Kerosene and Gaseous Fuels with a Natural and a Manufactured Mn–Fe-Based Oxygen Carrier, *Energy Fuels*, 2018, **32**(8), 8803–8816, DOI: 10.1021/acs.energyfuels.8b01588.

34 T. Mattisson, A. Lyngfelt and H. Leion, Chemical-Looping with Oxygen Uncoupling for Combustion of Solid Fuels, *Int. J. Greenhouse Gas Control*, 2009, **3**(1), 11–19, DOI: 10.1016/j.ijggc.2008.06.002.

35 G. Azimi, H. Leion, T. Mattisson and A. Lyngfelt, Chemical-Looping with Oxygen Uncoupling Using Combined Mn-Fe Oxides, Testing in Batch Fluidized Bed, *Energy Proc.*, 2011, **4**, 370–377, DOI: 10.1016/j.egypro.2011.01.064.

36 S. A. Theofanidis, C. Loizidis, E. Heracleous and A. A. Lemonidou, CO_2-Oxidative Ethane Dehydrogenation over Highly Efficient Carbon-Resistant Fe-Catalysts, *J. Catal.*, 2020, **388**, 52–65, DOI: 10.1016/j.jcat.2020.05.004.

37 D. S. Baser, Z. Cheng, J. A. Fan and L.-S. Fan, Codoping Mg-Mn Based Oxygen Carrier with Lithium and Tungsten for Enhanced C2 Yield in a Chemical Looping Oxidative Coupling of Methane System, *ACS Sustainable Chem. Eng.*, 2021, **9**(7), 2651–2660, DOI: 10.1021/acssuschemeng.0c07241.

38 Z. Yang, H. Li, H. Zhou, L. Wang, L. Wang, Q. Zhu, J. Xiao, X. Meng, J. Chen and F. Xiao, Coking-Resistant Iron Catalyst in Ethane Dehydrogenation Achieved through Siliceous Zeolite Modulation, *J. Am. Chem. Soc.*, 2020, **142**(38), 16429–16436, DOI: 10.1021/jacs.0c07792.

39 X. Qin, H. Wu, R. Wang, L. Wang, L. Liu, H. Li, B. Yang, H. Zhou, Z. Liao and F.-S. Xiao, Domino Catalysis for Selective Dehydrogenation of Ethane with Shifted Thermodynamic Equilibrium, *Joule*, 2023, 7(4), 753–764, DOI: 10.1016/j.joule.2023.03.004.

40 N. L. Galinsky, A. Shafiefarhood, Y. Chen, L. Neal and F. Li, Effect of Support on Redox Stability of Iron Oxide for Chemical Looping Conversion of Methane, *Appl. Catal., B*, 2015, **164**, 371–379, DOI: 10.1016/j.apcatb.2014.09.023.

41 D. Chacko, L. M. Neal, B. M. Lis, J. Liu, A. Pedersen, I. E. Wachs and F. Li, Effective COx Suppression by a $Na_4Mg(WO_4)_3$ Promoter in Chemical Looping Oxidative Dehydrogenation of Ethane, *ACS Catal.*, 2025, **15**(5), 3992–4006, DOI: 10.1021/acscatal.4c07851.

42 Y. Larring, C. Braley, M. Pishahang, K. A. Andreassen and R. Bredesen, Evaluation of a Mixed Fe–Mn Oxide System for Chemical Looping Combustion, *Energy Fuels*, 2015, **29**(5), 3438–3445, DOI: 10.1021/acs.energyfuels.5b00048.

43 Z. Sarshar, F. Kleitz and S. Kaliaguine, Novel oxygen carriers for chemical looping combustion: $La_{1-x}Ce_xBO_3$ (B = Co, Mn) perovskites synthesized by reactive grinding and nanocasting, *Energy Environ. Sci.*, 2011, **4**, 4258–4269.

44 F. Hao, Y. Gao, L. Neal, R. B. Dudek, W. Li, C. Chung, B. Guan, P. Liu, X. Liu and F. Li, Sodium Tungstate-Promoted $CaMnO_3$ as an Effective, Phase-Transition Redox Catalyst for Redox Oxidative Cracking of Cyclohexane, *J. Catal.*, 2020, **385**, 213–223, DOI: 10.1016/j.jcat.2020.03.022.

45 N. Galinsky, A. Mishra, J. Zhang and F. Li, $Ca_{1-x}A_xMnO_3$ (A = Sr and Ba) Perovskite Based Oxygen Carriers for Chemical Looping with Oxygen Uncoupling (CLOU), *Appl. Energy*, 2015, **157**, 358–367, DOI: 10.1016/j.apenergy.2015.04.020.

46 A. Abad, A. Filsouf, I. Adánez-Rubio, T. Mendiara, L. F. de Diego, M. T. Izquierdo, P. Gayán and J. Adánez, Chemical Looping with Oxygen Uncoupling of Biomass and Coal: Scaling-Up to 50 kWth Using a Copper-Based Oxygen Carrier, *Energy Fuels*, 2024, **38**(21), 21333–21344, DOI: 10.1021/acs.energyfuels.4c03173.

47 G. Azimi, H. Leion, M. Rydén, T. Mattisson and A. Lyngfelt, Investigation of Different Mn–Fe Oxides as Oxygen Carrier for Chemical-Looping with Oxygen Uncoupling (CLOU), *Energy Fuels*, 2013, **27**(1), 367–377, DOI: 10.1021/ef301120r.

48 K. Li, G. Li, Z. Zhao, X. Ding, N. Li, S. Ma and Y. Zhang, Biomass Based Oxygenates Modified Fe-Mn Oxide with Improved Surface Lattice Oxygen Mobility for the Chemical Looping-Oxidative Dehydrogenation of Ethane to Ethylene, *Fuel*, 2024, **364**, 131116, DOI: 10.1016/j.fuel.2024.131116.

49 S. Yusuf, V. Haribal, D. Jackson, L. Neal and F. Li, Mixed Iron-Manganese Oxides as Redox Catalysts for Chemical Looping–Oxidative Dehydrogenation of Ethane with Tailorable Heat of Reactions, *Appl. Catal., B*, 2019, **257**, 117885, DOI: 10.1016/j.apcatb.2019.117885.

50 S. Han, Y. Wang, Q. Jing, H. Wu, S. Pan and Z. Yang, Effect of the Cation Size on the Framework Structures of Magnesium Tungstate, $A_4Mg(WO_4)_3$ (A = Na, K), $R_2Mg_2(WO_4)_3$ (R = Rb, Cs), *Dalton Trans.*, 2015, **44**(12), 5810–5817, DOI: 10.1039/C5DT00332F.

51 D. K. Amarasinghe and F. A. Rabuffetti, Bandshift Luminescence Thermometry Using Mn^{4+}:$Na_4Mg(WO_4)_3$ Phosphors, *Chem. Mater.*, 2019, **31**(24), 10197–10204, DOI: 10.1021/acs.chemmater.9b03886.

52 Y.-B. Kang and I.-H. Jung, Critical Evaluations and Thermodynamic Optimizations of the MnO–Mn_2O_3–SiO_2 and FeO–Fe_2O_3–MnO–Mn_2O_3–SiO_2 Systems, *Metall. Mater. Trans. B*, 2017, **48**(3), 1721–1735, DOI: 10.1007/s11663-017-0953-5.

53 A. Muan and S. Somiya, The System Iron Oxide-Manganese Oxide in Air, *Am. J. Sci.*, 1962, **260**(3), 230–240, DOI: 10.2475/ajs.260.3.230.

54 Diagram 11088. https://phaseonline.ceramics.org/viewer/34199___11088 (accessed 2025-03-27).

55 T. Yamashita and P. Hayes, Analysis of XPS Spectra of Fe^{2+} and Fe^{3+} Ions in Oxide Materials, *Appl. Surf. Sci.*, 2008, **254**(8), 2441–2449, DOI: 10.1016/j.apsusc.2007.09.063.

56 E. S. Ilton, J. E. Post, P. J. Heaney, F. T. Ling and S. N. Kerisit, XPS Determination of Mn Oxidation States in Mn (Hydr)Oxides, *Appl. Surf. Sci.*, 2016, **366**, 475–485, DOI: 10.1016/j.apsusc.2015.12.159.